# Creep Rupture Mechanisms in Annealed and Overheated 7075 Al under Multiaxial Stress States

AHMADALI YOUSEFIANI, FARGHALLI A. MOHAMED, and JAMES C. EARTHMAN

The creep deformation and rupture behavior of annealed and overheated 7075 Al was investigated under uniaxial, biaxial, and triaxial stress states. Examinations of samples prior to and after testing using optical microscopy, scanning electron microscopy (SEM), and transmission electron microscopy (TEM) were also performed to develop a better understanding of the microstructural mechanisms governing this behavior. These observations combined with analyses of the test data indicate that annealed 7075 Al under present testing conditions exhibits characteristics of dislocation creep with a concomitant contribution from grain boundary sliding (GBS). By contrast, the results for overheated 7075 Al suggest that GBS is suppressed. This hypothesis is supported by observations of large particles at grain boundaries in the overheated microstructure and few or no particles at boundaries in the annealed microstructures. Rupture times for the different stress states were also compared with respect to four multiaxial stress parameters, each of which is linked to a particular physical mechanism that can facilitate creep rupture. It was found that creep rupture in annealed 7075 Al (regardless of sample orientation) is dominated by cavitation coupled with GBS. By contrast, the rupture behavior of overheated 7075 Al is consistent with a model that describes cavitation constrained by relatively uniform creep deformation in the matrix. Thus, the rupture findings also indicate that GBS is prevented in the overheated microstructure, while it gives rise to significant stress redistribution in the annealed microstructure.

## I. INTRODUCTION

UNIAXIAL stress conditions have commonly been employed in comprehensive studies concerning failure of engineering materials at high temperatures. These investigations have provided substantial information regarding the factors governing creep rupture. Different failure modes have been classified, and systematic descriptions for the mechanics and mechanisms of creep rupture have been well established.[1,2,3] It has been observed[4] that, for uniaxial creep conditions, a fundamental power law exists, which simply relates the time to rupture, $t_f$, and the applied stress, $\sigma$, as follows:

$$t_f = M\sigma^{-\chi} \qquad [1]$$

where $M$ and $\chi$ are stress-independent constants for a given material and testing condition.

In high-temperature applications, however, the majority of the components are subject to stress states varying in both time and position. Under such complex loading conditions, the stress used in Eq. [1] must be modified to correctly predict rupture time. Due to the difficulties in establishing stress distributions for creep deformation of multiaxially stressed components, the general effort has been geared toward obtaining a representative stress parameter, $\sigma_{\text{rep}}$, which is substituted for $\sigma$ in Eq. [1] and is used to forecast $t_f$ utilizing data from conventional uniaxial creep rupture tests. Table I describes several examples of such parameters expressed in terms of principal stresses, $\sigma_1 > \sigma_2 > \sigma_3$.

The majority of stress parameters developed for predicting creep life under multiaxial stress states are based on continuum mechanics approaches.[4–8] Multiaxial stress terms are combined in a weighted formula, and the relative contribution of each term is described by an adjustable factor, which is determined from data generated at different stress states (Eqs. [2] and [3]). The terms $M$ and $\chi = -\partial \log t_f/\partial \log \sigma$ are obtained from uniaxial creep rupture tests (Eq. [1]), and through analysis of experimental data, coefficients $\alpha$ or $\nu$ are adjusted to obtain the optimum correlation between the rupture time data for different stress states.

Multiaxial stress parameters advanced by the continuum mechanics approach may be utilized satisfactorily to predict the creep life of components. However, it should be considered that (1) determination of these parameters will require extensive multiaxial creep and rupture data, and (2) limited information is provided regarding the physical mechanisms involved in the creep rupture process. Such limitations can be overcome by alternatively using multiaxial stress parameters derived from mechanistic approaches. Distinguished by the fact that their determination does not involve adjustable terms, these stress parameters are each associated with a specific set of physical mechanisms that control the creep rupture process. The four different mechanistic parameters considered in the present work, the maximum principal stress, $\sigma_1$; the von Mises effective stress, $\sigma_e$; the principal facet stress, $\sigma_F$, and the constrained growth stress parameter, $\sigma_C$, are described briefly in Table I. In addition to predicting creep life of a component under multiaxial stress states, mechanistic stress parameters can be utilized to gain a better understanding of the physical processes governing the rupture process. Thus, the ability to identify representative

AHMADALI YOUSEFIANI, formerly Graduate Student Researcher with the Department of Chemical and Biochemical Engineering and Materials Science, University of California, Irvine, is now Senior Engineer/Scientist with the Space and Communications Group, The Boeing Company, Huntington Beach, CA 92647-2099. FARGHALLI A. MOHAMED and JAMES C. EARTHMAN, Professors, are with the Department of Chemical and Biochemical Engineering and Materials Science, University of California, Irvine, Ca 92697-2575.

Manuscript submitted December 15, 1999.

**Table I. Multiaxial Representative Stress Parameters**

| Representative Stress Parameters | | Description |
|---|---|---|
| $\sigma_{\text{rep}} = \alpha\sigma_1 + (1 - \alpha)\sigma_e$ | [2] | • continuum mechanics approach[5]<br>• $\sigma_1$ and $\sigma_e$ contribute independently and represent the driving force for diffusional cavitation and creep deformation processes, respectively<br>• $\sigma_e$ is the effective stress (defined in Eq. [5]) and $\alpha$ is a constant |
| $\sigma_{\text{rep}} = \sigma_1^{\nu/\chi}\,\sigma_e^{\frac{\chi-\nu}{\chi}}$ | [3] | • continuum mechanics approach[6,7]<br>• contributions of different processes to creep rupture, driven by $\sigma_1$ and $\sigma_e$, are considered to be interdependent<br>• $\nu$ is a constant |
| $\sigma_{\text{rep}} = \sigma_1$ | [4] | • based on early multiaxial creep rupture studies[18]<br>• applied under the condition of the progressive development of a homogeneous distribution of cavities at a level microscopically visible from the onset of testing |
| $\sigma_{\text{rep}} = \sigma_e = \sqrt{\dfrac{(\sigma_1 - \sigma_2)^2 + (\sigma_2 - \sigma_3)^2 + (\sigma_1 - \sigma_3)^2}{2}}$ | [5] | • based on early multiaxial creep rupture studies[18]<br>• applied under the condition that no significant cavitation occurs in samples other than that observed in the close vicinity of the rupture surface |
| $\sigma_{\text{rep}} = \sigma_C = \sigma_1\sigma_e^{n-1}$ | [6] | • based on a cavity growth model developed by Rice[19]<br>• utilized for conditions where grain boundary cavitation is constrained by continuum creep rate of the surroundings (Section III-C)<br>• $n$ is the creep exponent |
| $\sigma_{\text{rep}} = \sigma_F = 2.24\sigma_1 - 0.62(\sigma_2 + \sigma_3)$ | [7] | • applicable for situations where cavitation is coupled with highly localized deformation processes, such as GBS[20] |

multiaxial stress parameters from a knowledge of underlying mechanisms offers considerable advantages, in addition to eliminating the need for a large number of multiaxial experiments that are both expensive and time consuming.

Over the years, high-strength aluminum alloys have successfully been used as structural materials in aerospace, transportation, and many other industries. Their utilization for applications requiring elevated temperature performance depends strongly on the understanding of their creep and rupture characteristics under multiaxial loading conditions. The present investigation examines the multiaxial creep rupture behavior of a representative high-strength Al alloy (7075 Al), utilizing a general approach in which the validity of the aforementioned mechanistic criteria is determined using stress state as a variable. Two microstructures were examined, one which results from a relatively standard annealing treatment and one that results when the alloy is taken to a substantially higher annealing temperature. The creep deformation and rupture results obtained for the two different microstructures were then used to characterize the mechanisms controlling high-temperature rupture in the present alloy.

## II. EXPERIMENTAL PROCEDURES

The commercial 7075 Al alloy used in the present work was received as 4.5-cm-thick rolled plates in the T6 condition. Samples were either annealed at 723 K or overheated at 823 K for 4 hours, air cooled to room temperature, and kept there for at least 1 week before testing. Creep tests were conducted in air under isothermal/isostress conditions, with the temperature maintained at 648 ± 2 K. Annealed samples were machined along two orientations, with their long axis parallel to either the longitudinal (designated as 7075 Al-L) or the long transverse (designated as 7075 Al-LT) rolling direction. Overheated samples were only machined with their long axis parallel to the longitudinal rolling direction (designated as 7075 Al-OH).

Three types of specimens, each corresponding to a different stress state, were utilized in this investigation (Table II). Uniaxial stress state was obtained using conventional smooth cylindrical creep specimens ($\sigma_1 = \sigma$, $\sigma_2 = \sigma_3 = 0$). A Bridgman circular notched tensile bar was applied to produce a triaxial state of stress. Finite element calculations reported for this sample geometry under creep conditions[9] indicate that the stresses across the notch become uniform very early in the life of the specimen. Afterward, the stress state in the Bridgman notch geometry is essentially constant and can be approximated by $\sigma_1 = 2.7\ \sigma_{\text{nom}}$ and $\sigma_2 = \sigma_3 = \sigma_1/3$. The state of biaxial shear was achieved using a modified double shear specimen.[10] The generated shear stress is highest at

**Table II. Specimen Geometry and Corresponding Stress States**

| Geometry and Stress State | Stress Analysis |
|---|---|
| 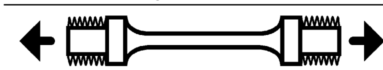<br>Uniaxial Tension | $\sigma_{\text{app}} = F/A_{\text{min}}$<br>$\sigma_1 = \sigma_{\text{app}}$<br>$\sigma_2 = 0,\ \sigma_3 = 0$ |
| 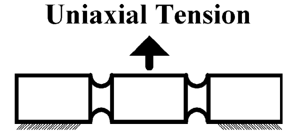<br>Biaxial Shear | $\tau_{\text{max}} \cong F/2A_{\text{min}}$<br>$\sigma_1 = \tau_{\text{max}}$<br>$\sigma_2 = 0,\ \sigma_3 = -\tau_{\text{max}}$ |
| 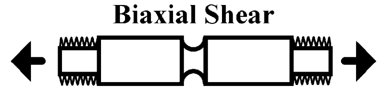<br>Triaxial Tension | $\sigma_{\text{nom}} = F/A_{\text{max}}$<br>$\sigma_1 = 2.7\ \sigma_{\text{nom}}$<br>$\sigma_2 = \sigma_3 = 0.33\sigma_1$ |

the minimum cross-sectional area of the notches. Assuming no bending moment is present in the notches, and stress concentrations are relaxed early in the life of the specimen, the stress state for this specimen may be characterized by $\sigma_1 = -\sigma_3 \approx \tau_{max}$ and $\sigma_2 = 0$.[10,11]

Microstructural examinations were conducted through the use of both optical and electron microscopy. Optical microscopy was utilized to reveal (1) grain size/morphology and particle size/distribution in 7075 Al (as-received and heat-treated conditions) and (2) the extent/distribution of cavities in samples tested to failure. Samples were polished using conventional metallographic techniques and etched using Keller's reagent where necessary. Transmission electron microscopy (TEM) examinations, which were performed to investigate substructural features in the alloy, were conducted using a PHILIPS* CM20 transmission electron microscope operating at 200 kV. Thin foils were mechanically polished to about 100 $\mu$m and twin-jet polished using a 25 pct nitric acid-75 pct methanol solution, maintained below 240 K. Scanning electron microscopy (SEM) was used to provide information regarding (1) the morphological features of the fracture surfaces, (2) cavity nucleation sites, (3) chemical compositions of second-phase particles, and (4) grain structure and precipitate-free zones (PFZs) in the alloy. The SEM investigations were performed using a PHILIPS XL30 scanning electron microscope, with an energy dispersive spectroscopy (EDS) attachment.

*PHILIPS is a trademark of Philips Electronic Instruments Corp., Mahwah, NJ.

## III. EXPERIMENTAL RESULTS

### A. *Microstructure*

Figure 1 illustrates and compares the microstructural features observed in 7075 Al in the as-received (top row), annealed (middle row), and overheated (bottom row) conditions. The triplanar optical micrographs show the etched (left column) and polished (right column) microstructures in the longitudinal and transverse directions.

Partially recrystallized grains, elongated in the rolling direction, are typical of the alloy in the T6 (as-received) condition (Figure 1(a)). Figure 1(b), which shows the polished surface of the alloy in the as-received condition, reveals the size and distribution of the insoluble second-phase constituent particles. During prior working operations, particles break down and roughly align as stringers in the rolling direction. The EDS analysis indicated that the majority of these particles, with sizes ranging between 2 and 10 $\mu$m, are Fe-bearing phases; however, Si-bearing particles were also identified. Due to its very low solid solubility, most of the Fe present within the Al matrix appears as intermetallic second-phase particles (in combination with other elements). Insoluble phases that have been observed in 7075 Al are mainly $Al_7Cu_2Fe$, $Al_{23}CuFe_4$, $Al_6Fe$, $Mg_2Si$, and $(FeMnCr)_3SiAl_{12}$.[12,13]

The two types of heat treatments conducted prior to testing resulted in remarkably different microstructures (Figures 1(c) through (f)). While both treatments (annealing and overheating) served the common purposes of relieving strain-hardening effects, inducing recrystallization, and stabilizing the microstructure, overheating also resulted in grain growth and the elimination of dislocation substructures. Figure 1(c) shows the etched microstructure after annealing. Due to the dense precipitation that resulted from annealing, no grain contrast could be produced through etching. Figure 1(d) indicates that annealing results in the dissolution of existing phases and subsequent precipitation of slightly coarser (3 to 15 $\mu$m), more homogeneously distributed second-phase constituents compared to those found in the as-received condition. By contrast, overheating 7075 Al produces a fully recrystallized, coarse-grained microstructure (Figure 1(e)), with a completely heterogeneous distribution of coarse (5 to 25 $\mu$m) second-phase constituents within the grains (Figure 1(f)) and a dense population of large precipitates at the grain boundaries.

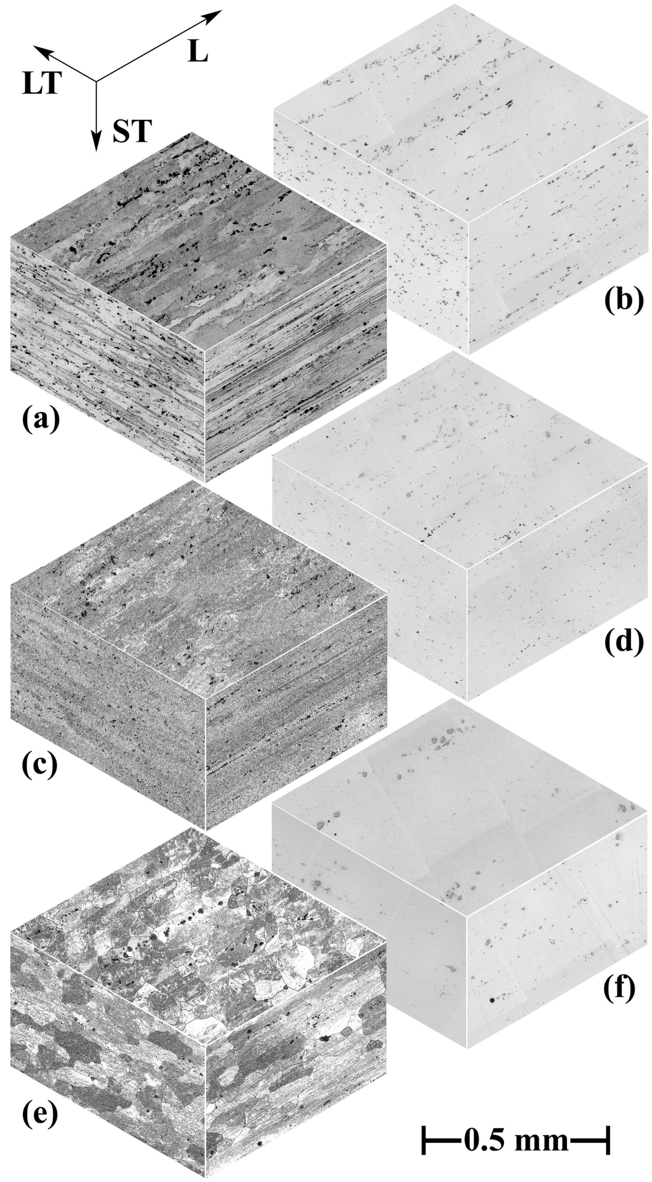


Fig. 1—Triplanar optical micrographs showing microstructural features observed in 7075 Al. As-received condition (*a*) etched and (*b*) polished; annealed condition (*c*) etched and (*d*) polished; and overheated condition (*e*) etched and (*f*) polished.

Resolving grain boundaries in the annealed microstructure was not possible using optical microscopy. However, the presence of relatively wide PFZs and constituent particles

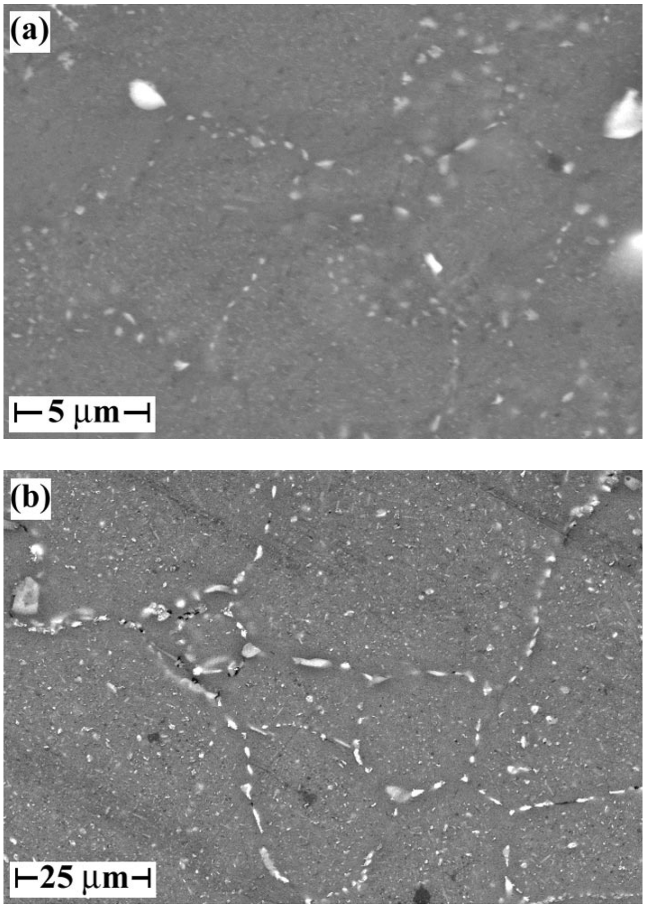


Fig. 2—SEM micrographs revealing grain structure, grain boundary precipitates, and PFZs in (*a*) 7075 Al-L, $\varepsilon = 0.137$, $\sigma = 10.5$ MPa; and (*b*) 7075 Al-OH, $\varepsilon = 0.140$, $\sigma = 10.3$ MPa. Representative samples shown in this figure were tested under uniaxial tension.

located preferentially on the grain boundaries made it possible to observe grain size and morphology by SEM examination in the backscatter mode following creep deformation (Figure 2). Measurements on representative annealed samples, deformed to approximately 15 pct at different stress levels, revealed a recrystallized, fairly equiaxed grain morphology, with an average spatial grain size $d$ ($d = 1.74\bar{L}$, where $\bar{L}$ is the mean linear intercept) of $10 \pm 1$ $\mu$m. The size of the constituent particles ranged from about 0.1 to 0.3 $\mu$m, and the average width of the PFZs was determined to be $0.5 \pm 0.1$ $\mu$m. The overheated samples exhibited an average equiaxed grain size of $80 \pm 5$ $\mu$m, PFZs with an average width of $3 \pm 0.5$ $\mu$m, and platelets of constituent particles decorating the grain boundaries and varying in size from 0.8 to 6 $\mu$m along the long axis.

The TEM micrographs included in Figure 3 illustrate and compare the substructural features observed in the annealed (top row) and overheated (bottom row) conditions. Figures 3(a) and (b) indicate that annealed 7075 Al contains the following: (1) a well-defined relatively elongated subgrain structure; (2) small amounts of Cr-bearing dispersoids, most likely $Al_{18}Mg_3Cr_2$;[12] and (3) rodlike $MgZn_2$, which resulted from the coarsening (during annealing) of the Guinier–Preston (G–P) zones present in the T6 condition. In contrast, Figures 3(c) and (d) reveal the absence of subgrains and the presence of much coarser precipitates in the overheated condition. Dispersoids, such as those observed in the annealed condition, are present intentionally to control the grain structure. They are virtually insoluble and resistant to coarsening under normal heating conditions. However, the overheating treatment, which takes place at 823 K, is well above conventional solutionizing temperatures and into the region of incipient melting (805 K). This is expected to have a pronounced effect on the microstructure of the alloy and may have led either to the dissolution or to significant coarsening of the Cr-bearing dispersoids, which is most likely the reason for both the absence of dislocation substructures and the significant grain growth for the overheated condition. The morphological differences in the constituent particles observed using SEM (Figure 2) show similar characteristics. The particles distributed along the boundaries in the annealed condition (Figure 2(a)) are relatively small and well rounded (representing the Cr-bearing dispersoids) on some boundaries and nonexistent on others. Constituent particles decorating the grain boundaries in the overheated condition (Figure 2(b)) are much coarser and plateletlike (corresponding to coarsened $MgZn_2$ precipitates) and appear to be uniformly present on all boundaries.

The preceding results illustrate the microstructural similarities and differences observed in 7075 Al under various heat treatments. However, it is important to further examine the fine grain structure developed as a result of annealing. As noted earlier, revealing the grain structure of the annealed samples requires slight creep deformation. The TEM observations indicate that annealing alone has very little influence on the as-received microstructure. Its effect seems to be limited to the precipitation of dissolved constituents, and even though recrystallization may have taken place, no appreciable difference in the (sub)grain structure was observed. Therefore, the evolution of the fine-grained structure in the annealed samples could not have occurred as a result of static recrystallization. Following appropriate thermomechanical treatments, it is possible to produce a fine grain structure in 7075 Al, either through static recrystallization prior to creep deformation[14] or by dynamic/continuous recrystallization occurring during the early stages of creep deformation.[15,16] The exact determination of the process that has led to the development of a fine grain structure in the annealed samples is beyond the scope of this investigation. However, it seems that continuous recrystallization takes place dynamically in the very early stages of creep deformation based on the observations made in this study. Most probably the subgrains (with low angle boundaries) present in the alloy coarsen as creep deformation proceeds, and similar to observations made elsewhere,[15,16] the subgrains increase in misorientation, due to concurrent slip and/or grain boundary sliding (GBS), until the development of high angle boundaries is complete.

B. *High-Temperature Deformation*

Due to the complexities introduced by the notches, analysis of creep deformation in the biaxial and triaxial specimens has not been included in the present investigation. However, the standard data obtained under uniaxial conditions have been used to study and analyze creep behavior in 7075 Al. Typical examples of creep curves obtained under uniaxial conditions are shown in Figure 4, where the true tensile strain, $\varepsilon$, is plotted against time, $t$. The applied stress ranged

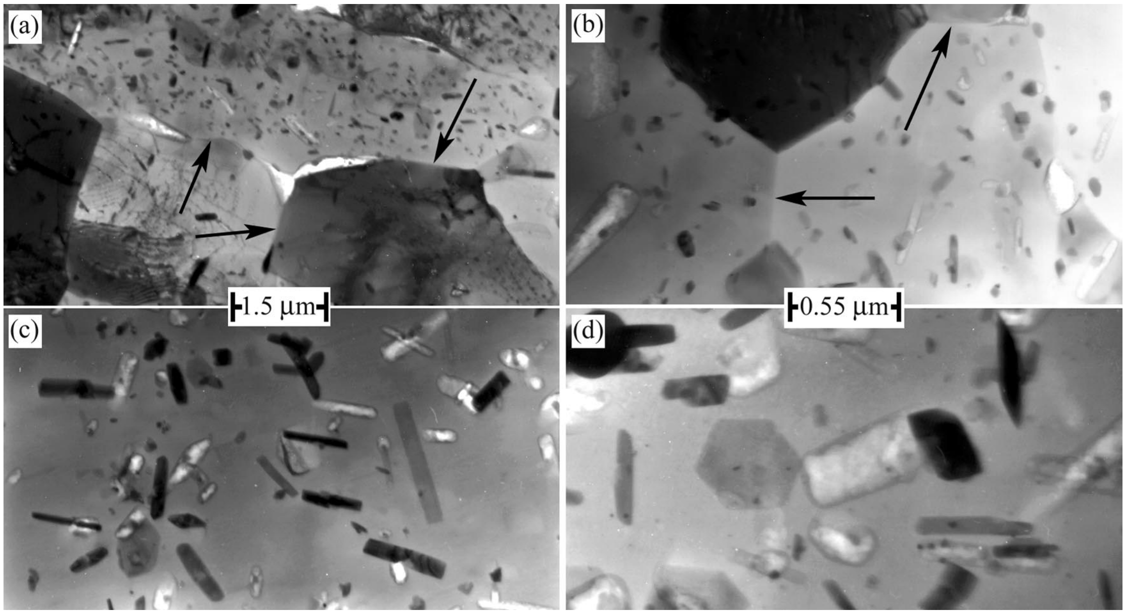


Fig. 3—TEM micrographs revealing the substructural features observed in (*a*) annealed 7075 Al, (*b*) annealed 7075 Al at high magnification, (*c*) overheated 7075 Al, and (*d*) overheated 7075 Al at high magnification. Arrows indicate particle-free boundaries present in the annealed microstructure.

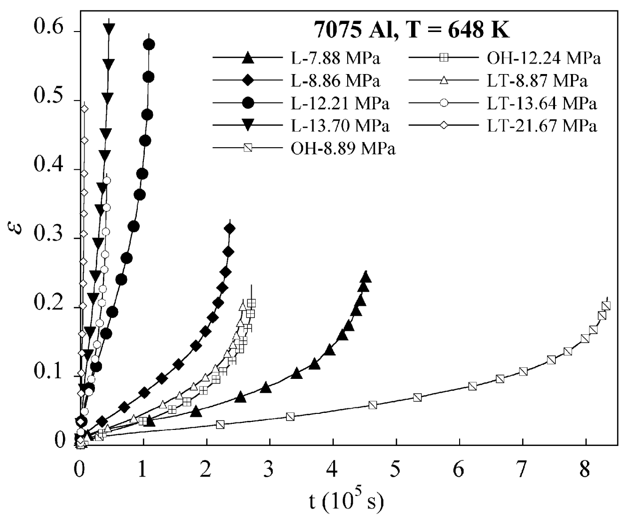


Fig. 4—Typical creep curves showing true tensile strain, $\varepsilon$, as a function of time, $t$. Samples were tested under uniaxial conditions.

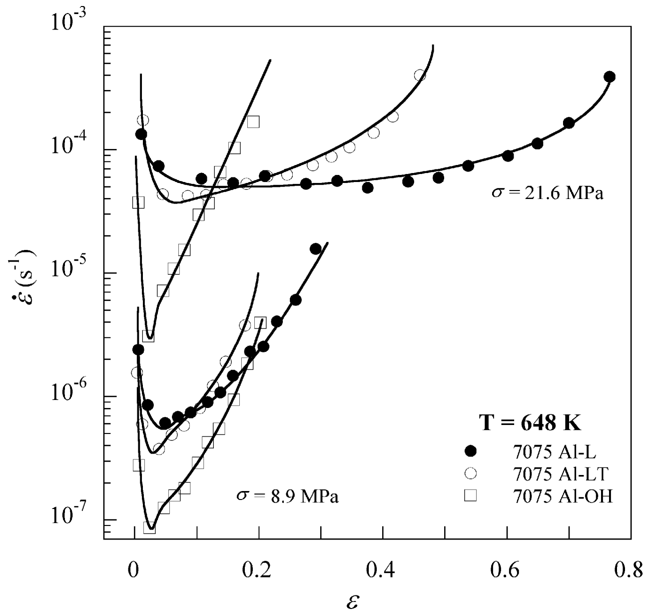


Fig. 5—Results of uniaxial tests conducted on samples at low and relatively high stresses. Strain rate, $\dot{\varepsilon}$, is plotted against true tensile strain, $\varepsilon$.

from 8 to 30 MPa, covering close to four orders of magnitude of strain rate. It should be noted that the instantaneous strain, which generally increased with increasing applied stress, was subtracted from the total strain. Therefore, the creep curves shown in Figure 4 start at the origin of the coordinates and represent only the strain due to creep. Figure 5, in which $\varepsilon$ is plotted against strain rate, $\dot{\varepsilon}$, includes results from samples tested at low and relatively high stresses, providing additional means of interpreting and comparing the creep behavior under different conditions. Regardless of the type of heat treatment or sample orientation, results indicate that, in general, all creep curves exhibit a normal primary stage ($d\dot{\varepsilon}/dt < 0$), followed by a very limited secondary stage of steady-state creep rate ($d\dot{\varepsilon}/dt = 0$), and an extended tertiary stage ($d\dot{\varepsilon}/dt > 0$) that accounts for most of the sample life. Due to the limited extent of the secondary stage (evident in Figure 5), where applicable, minimum creep rate has been used instead of steady state. Examination of the creep curves in Figure 5, as well as those not shown, indicates the presence of a very sharp creep-rate minimum in 7075 Al-OH at all stress levels. While 7075 Al-L and 7075 Al-LT show a similar, but less accentuated, creep-rate minimum at the lowest stress levels, they generally exhibit a smooth secondary stage transition and approach an almost ideal steady-state behavior at the highest stress levels tested.

The differences in creep ductility become apparent in Figure 6, where the rupture strain, $\varepsilon_f$, is plotted against the applied stress. While creep ductility remains relatively constant with increasing stress levels (increasing slightly at

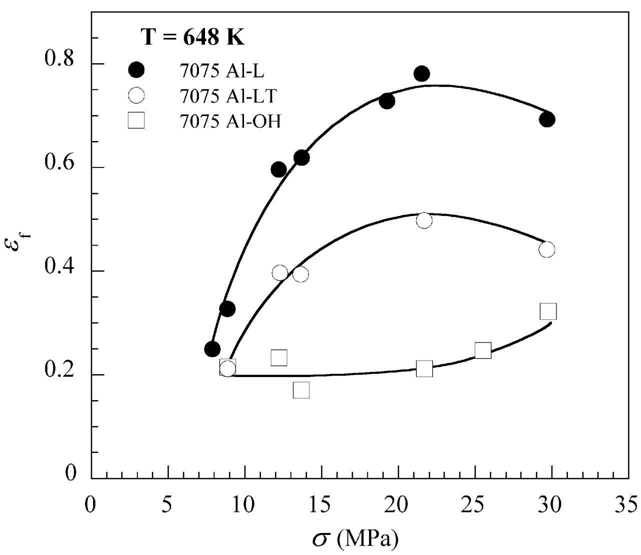


Fig. 6—Rupture strain, $\varepsilon_f$, as a function of the applied stress, $\sigma$, for samples tested to failure under uniaxial conditions.

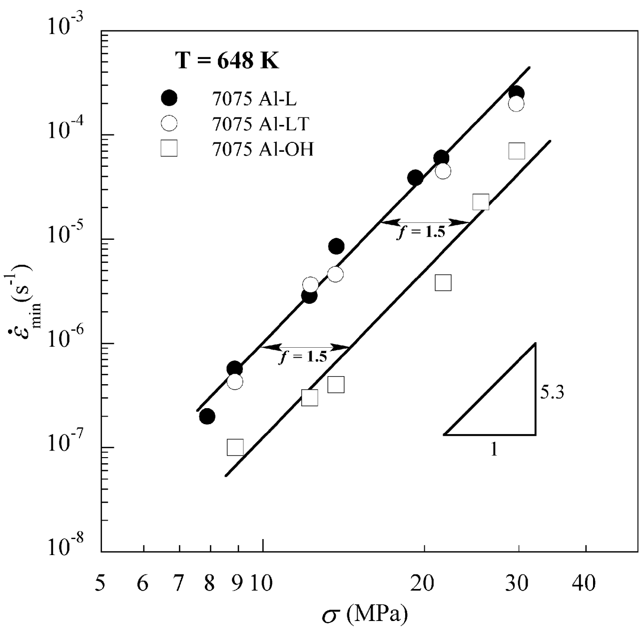


Fig. 7—The stress dependence of minimum creep rate for 7075 Al tested at 648 K.

the highest stress) for 7075 Al-OH, it is evident that both 7075 Al-L and 7075 Al-LT show an increase in ductility, which reaches a maximum and ultimately decreases at high stresses. The overall creep ductility is highest in 7075 Al-L, followed by 7075 Al-LT and 7075 Al-OH.

The stress dependence of minimum (or steady-state) creep rate can often be well approximated by a power law, which for practical purposes can be described in the following simple form (Norton's law):

$$\dot{\varepsilon}_{min} = A\sigma^n \qquad [8]$$

where $A$ is a temperature- and microstructure-dependent constant, and $n$ is the stress exponent for creep, normally ranging from 3 to 8, depending on the type of alloy and the governing creep mechanism. Figure 7, in which $\dot{\varepsilon}_{min}$ has been plotted

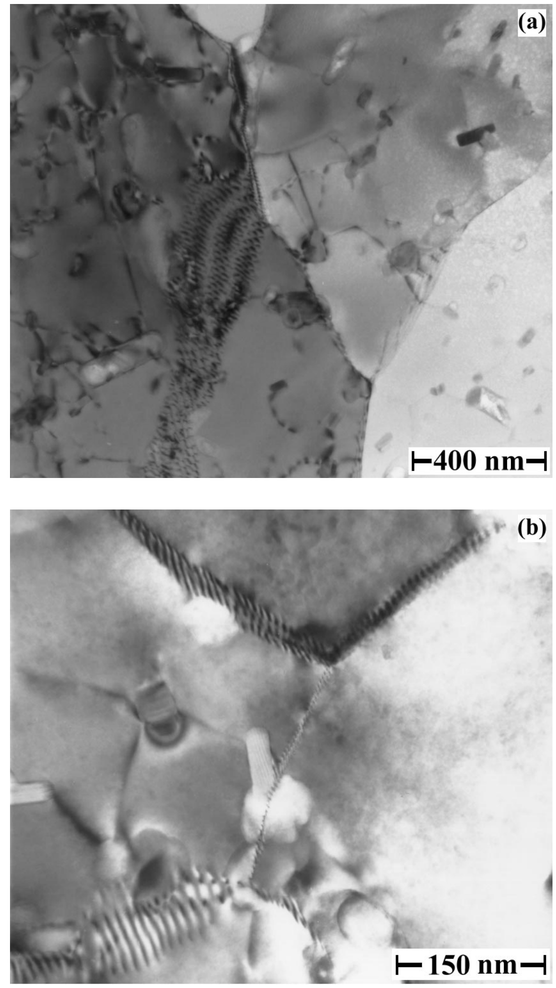


Fig. 8—TEM micrographs representing typical substructural observations made in 7075 Al. (*a*) Dislocation networks, and dislocation jogs, loops, and dipoles in the interior of the subgrains. (*b*) Arrays of dislocations forming simple sub-boundaries. The sample was tested under uniaxial tension ($\varepsilon \cong 0.2$ and $\sigma = 12.5$ MPa).

against $\sigma$ on a double logarithmic scale, can be utilized to investigate the creep behavior in 7075 Al. The straight fit through the data obtained at 648 K indicates that creep behavior in the alloy, over the range of strain rates investigated, obeys Eq. [8]. Regardless of heat treatment or sample orientation, results show that the value of the stress exponent $n = (\partial \ln \dot{\varepsilon}_{min}/\partial \ln \sigma)_T$ for 7075 Al is approximately 5.3. Results also indicate that creep strength in 7075 Al-OH is almost an order of magnitude higher than that of 7075 Al-L and 7075 Al-LT, which show identical stress dependencies.

In order to investigate the occurrence of dislocation activity during creep deformation, additional uniaxial tests were conducted at intermediate stress levels. The tests were terminated at $\varepsilon \cong 0.2$, and the representative samples were cooled rapidly under load to preserve any substructural development. Thin foils were prepared parallel to the tensile axis from regions located in the most highly deformed sections of the specimens. The TEM micrographs shown in Figure 8 represent the typical observations made in the alloy. Figure 8(a) indicates the presence of dislocation networks, and dislocation jogs, loops, and dipoles in the interior of the subgrains. Figure 8(b), at very high magnification, reveals arrays of dislocations forming simple sub-boundaries.

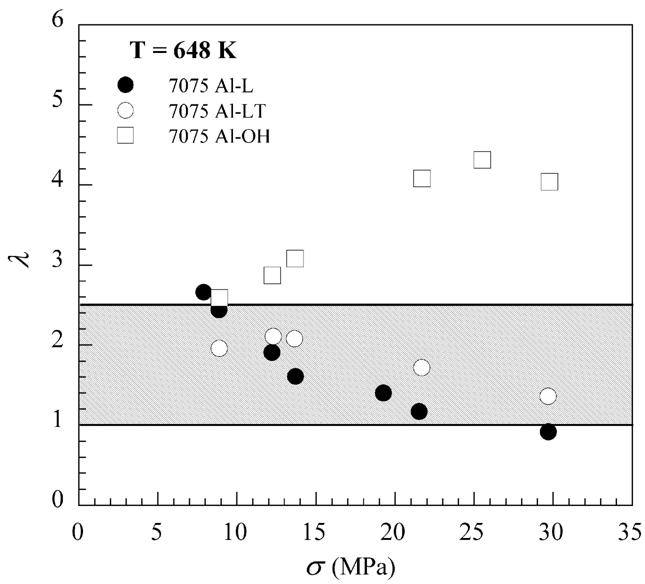


Fig. 9—Damage tolerance parameter, $\lambda$, as a function of the applied stress for samples tested under uniaxial tension.

C. *High-Temperature Rupture*

The creep-damage tolerance, $\lambda = \varepsilon_f/(\dot{\varepsilon}_{\min} t_f)$, is a parameter used to measure the tolerance of a creeping material with respect to strain concentrations.[2] It has been shown that failure occurs by creep cavitation for $1 < \lambda < 2.5$, and when $\lambda$ takes on larger values (commonly greater than 5), microstructural degradation becomes the dominant damage mechanism. At intermediate levels, the likelihood of an interaction between the two mechanisms exists. Such a situation has been investigated in detail,[17] using a two-state-variable damage approach. In this way, $\lambda$ may be used to identify mechanisms controlling creep rupture. Uniaxial creep rupture data obtained for 7075 Al are used in Figure 9 to plot the damage tolerance parameter against the applied stress. It can be seen in this figure that the data for 7075 Al-L and 7075 Al-LT fall within the $1 < \lambda < 2.5$ (shaded) region. The $\lambda$ values for 7075 Al-OH, on the other hand, range from a minimum of 2.6 at lower stresses to an average of 4.2 at intermediate and high stresses. Hence, $\lambda$ values indicate that 7075 Al-L and 7075 Al-LT predominantly fail by creep cavitation, while other modes of microstructural degradation, such as particle coarsening, have a significant role in the rupture of 7075 Al-OH.

Results of early multiaxial creep rupture studies[18] conducted on a variety of metals and alloys suggested that creep life under multiaxial stress states can generally be predicted by either $\sigma_1$ or $\sigma_e$. For example, copper, NIMONIC* 75, and Mo steel were tested under multiaxial stresses at 523, 923, and 823 K, respectively. It was found that the specimens progressively develop a homogeneous distribution of cavities at a level microscopically visible from the onset of testing. The rupture times for these samples were correlated better by $\sigma_1$ as the representative stress parameter in Eq. [1], as opposed to $\sigma_e$. On the other hand, the better representative parameter was determined to be $\sigma_e$ for Al alloy RR59, 0.2 pct C steel, and a Mg alloy tested at 473, 723, and 293 K, respectively. The samples in this case exhibit practically no cavitation other than that observed in the close vicinity of the rupture surface. However, it has been observed over time that the most accurate representative stress parameters depend on both $\sigma_1$ and $\sigma_e$.[4,6–8] Nevertheless, these parameters symbolize extremes of material behavior and were consequently considered in the present investigation.

*NIMONIC is a trademark of INCO Alloys International, Inc., Huntington, WV.

The constrained growth stress parameter, which is based on a cavity growth model developed originally by Rice,[19] and later modified by Riedel,[1] can be utilized for conditions where grain boundary cavitation is constrained by the continuum creep rate of the surroundings. In the constrained limit, the model estimates the cavity growth rate by

$$\dot{R} = 0.13\dot{\varepsilon}_e a\left(\frac{b}{R}\right)^2 \frac{\sigma_1 - (1 - \omega)\sigma_0}{\sigma_e} \qquad [9]$$

where $R$ is the radius of the cavities (assumed to have all nucleated upon loading) with a uniform spacing equal to $b$, $a$ is the diameter of a cavitating grain boundary facet, $\omega = (2R/b)^2$ is the area fraction of cavitated grain boundary, $\dot{\varepsilon}_e = A\sigma_e^n$ is the effective strain rate in the remote creeping material, $A$ is a temperature- and microstructure-dependent constant, $n$ is the stress exponent for power-law creep, and $\sigma_0 = 2\gamma_s \sin \psi/R$ is the sintering stress ($\gamma_s$ is the surface free energy and $\psi$ is the equilibrium tip angle of the cavities). Neglecting $\sigma_0$, which is reasonable due to the relatively large cavity sizes observed in 7075 Al, and substituting for the effective strain rate gives the growth rate in the following simplified form: $\dot{R} = B\sigma_1\sigma_e^{n-1}$, where $B = 0.13Aa(b/R)^2$. Assuming only a small fraction of $t_f$ is involved in the final stages of failure (microcrack interlinkage and propagation), the rupture time will be governed by the cavity growth rate. Therefore, it follows that $t_f \propto (\sigma_1\sigma_e^{n-1})^{-1}$ under conditions of constrained cavity growth, and $\sigma_C = \sigma_1\sigma_e^{n-1}$ (Table I).

The principal facet stress parameter, $\sigma_F$ (Table I), was derived for situations where cavitation is coupled with highly localized deformation processes, such as GBS.[20] During sliding, shear stresses on inclined boundaries are relieved, giving rise to a redistribution of stresses to transverse boundaries that cavitate leading to rupture. The average tensile stress on grain boundary facets perpendicular to $\sigma_1$ is therefore amplified, and it is suggested that this enhanced stress level drives the rupture process.

High-temperature rupture data for the alloy are presented in Figure 10. The plots compare each of the representative stress parameters with respect to rupture time on a double logarithmic scale. Using the general form of Eq. [1], a regression analysis was applied to calculate the least-squares fit through the rupture data fields for all three stress states. The best fit and the corresponding correlation coefficients, as shown in the figure, can be used to accurately determine the validity of each representative stress parameter. The parameter that brings the data closest to a single line would therefore be best for predicting lifetime under multiaxial stress states. The superior correlation of the principal facet stress parameter for 7075 Al-L ($R^2 = 0.96$) and 7075 Al-LT ($R^2 = 0.95$) is clearly evident in Figure 10. However, it can be seen that $\sigma_C$ ($R^2 = 0.96$) correlates the rupture time best in the case of 7075 Al-OH, bringing all of the rupture data onto a single curve. It is important to note that, while the slope of the fit through the data is approximately $-1$ in

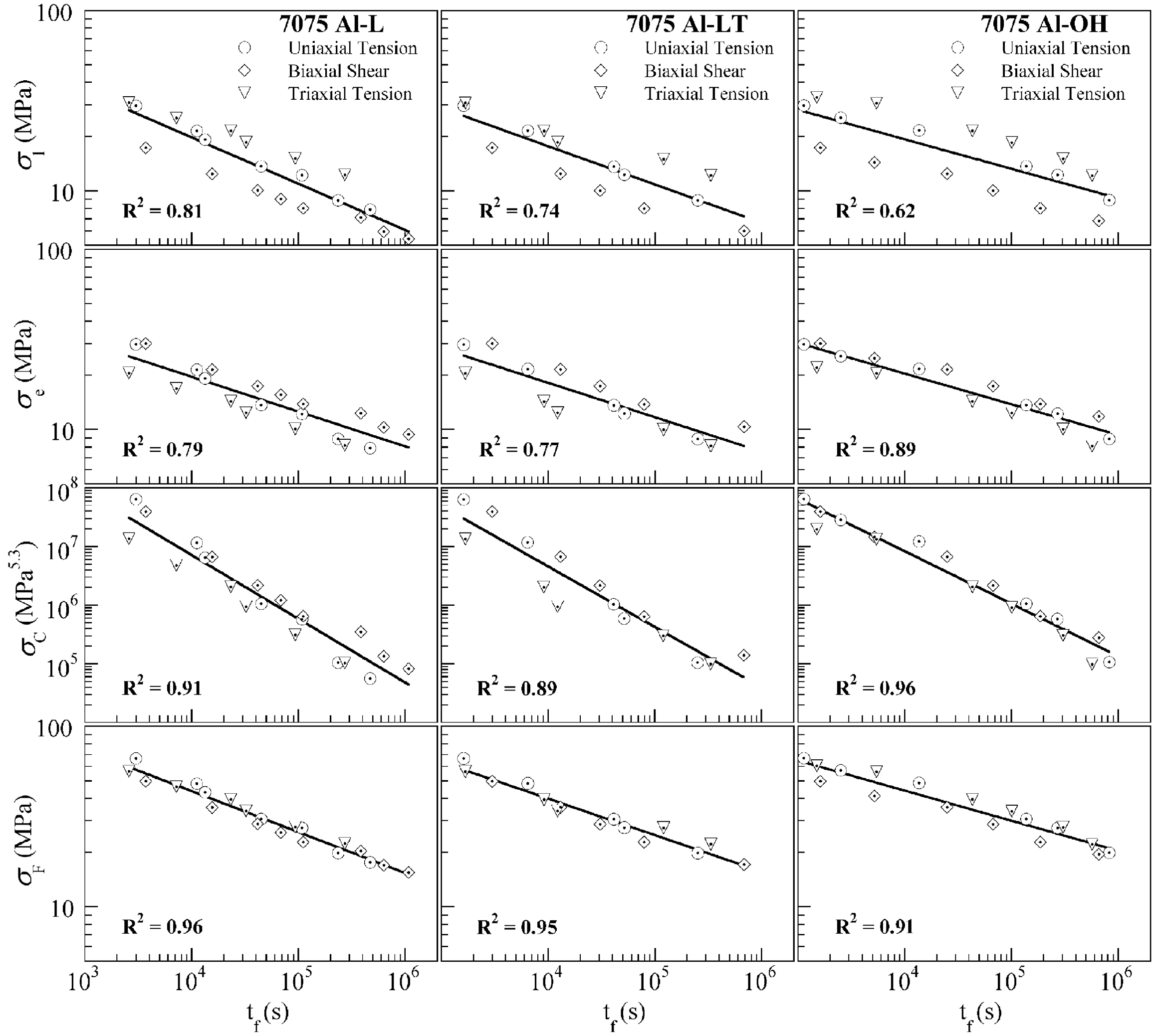


Fig. 10—High-temperature multiaxial rupture data for 7075 Al. The plots compare each of the representative stress parameters with respect to ruptur e time on a double logarithmic scale. The best fit and the corresponding correlation coefficients are also included.

all conditions using $\sigma_C$, the parameter fails to satisfactorily correlate the data for 7075 Al-L and 7075 Al-LT.

Figure 11, which shows the polished longitudinal cross sections of specimens tested to rupture under uniaxial conditions, illustrates and compares the cavitational features observed in 7075 Al-L (top row), 7075 Al-LT (middle row), and 7075 Al-OH (bottom row). The influence of stress level on cavitation behavior of the alloy may also be investigated by comparing samples tested at high stresses (left column) with those tested at low stresses (right column). Each image is a montage of several optical micrographs, covering a large area of the polished cross section in the vicinity of the rupture surface. With this perspective, both the deformation profile and cavitating regions away from the tip can be studied and compared. Examination of Figure 11 reveals that (1) widespread cavitation occurs in all samples and is not limited to regions near the rupture surface; (2) the extent of cavitation decreases with increasing stress levels; (3) cavity distribution is more homogeneous at lower stresses, with blunt microcracks that developed due to cavity coalescence being clearly visible; (4) cavity morphology changes at higher stresses, appearing more elongated in the direction of the tensile axis; and (5) necking becomes more prominent with increasing stress level. It is also evident that the overall extent of cavitation damage in 7075 Al-OH (Figures 11(e) and (f)) is significantly greater than that in 7075 Al-L and 7075 Al-LT (Figures 11(a) through (d)) when compared at similar stress levels. Similar observations and trends can be noted for the optical micrographs shown in Figure 12, which compare 7075 Al-L (left column) and 7075 Al-OH (right column) tested under triaxial tension (top row) and biaxial shear (bottom row). Samples chosen for Figure 12 were tested at intermediate levels (within the range of applied stresses for each state) and represent the general observations. It should be noted that the change in cavity morphology observed might be assumed to have originated from a transition in the dominant high-temperature rupture mechanism. However, the results shown in Figure 10 indicate that such an assumption is unfounded, since each of the corresponding stress parameters ($\sigma_F$ or $\sigma_C$) correlates all the rupture data over the entire stress range, depending on the sample (annealed or overheated). During creep rupture, different mechanisms typically occur in a coupled manner, with each being dominant for a certain fraction of the creep life.[2] While a certain mechanism, governed by the correlating parameter, may predominate most of the rupture time, the

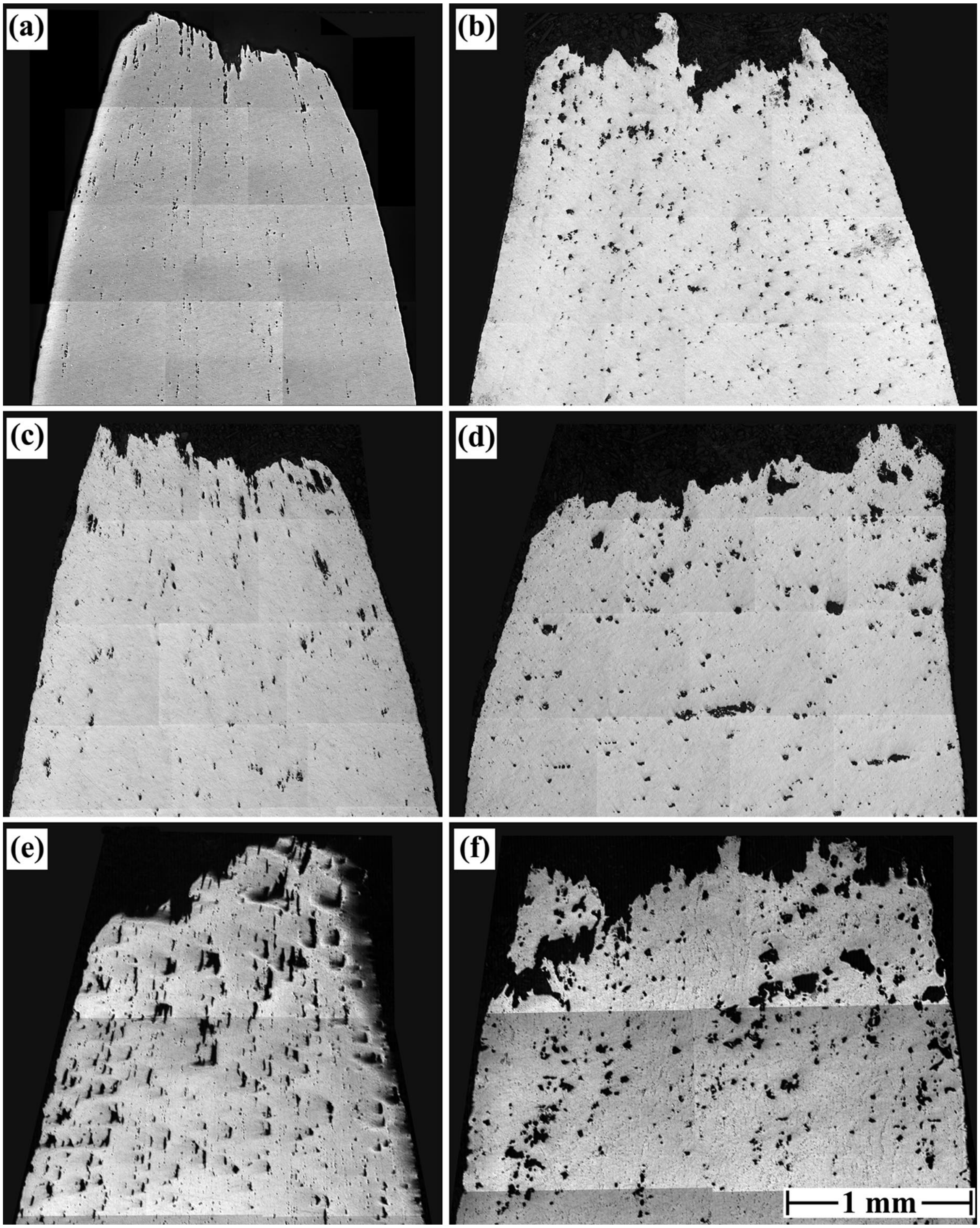


Fig. 11—Polished longitudinal cross sections of specimens tested to rupture under uniaxial conditions. (*a*) 7075 Al-L, $\sigma$ = 19.25 MPa; (*b*) 7075 Al-L, $\sigma$ = 8.86 MPa; (*c*) 7075 Al-LT, $\sigma$ = 21.60 MPa; (*d*) 7075 Al-LT, $\sigma$ = 8.87 MPa; (*e*) 7075 AL-OH, $\sigma$ = 21.70 MPa; and (*f*) 7075 Al-OH, $\sigma$ = 10.54 MPa. Each image is a montage of several optical micrographs, covering a large area near the rupture surface.

strain to failure and/or the final rupture mode may be facilitated by a different process. In most cases of extensive cavitation, void growth by creep deformation only becomes dominant in the final stages of rupture.

Detailed examination of the polished longitudinal cross sections of specimens tested to rupture were conducted at relatively high magnification using SEM. Typical observations made in different samples (7075 Al-L in Figures 13(a) and (b), 7075 Al-OH in Figure 13(c), and 7075 Al-LT in Figure 13(d)) indicate that the majority of cavities form at large second-phase constituent particles. The representative SEM micrographs included in Figures 13(a) through (d) show samples tested at intermediate stress levels, with regions of examination located at least 1.5 mm away from the rupture surface. These figures illustrate the following general observations: (1) aligned cavities, which had formed

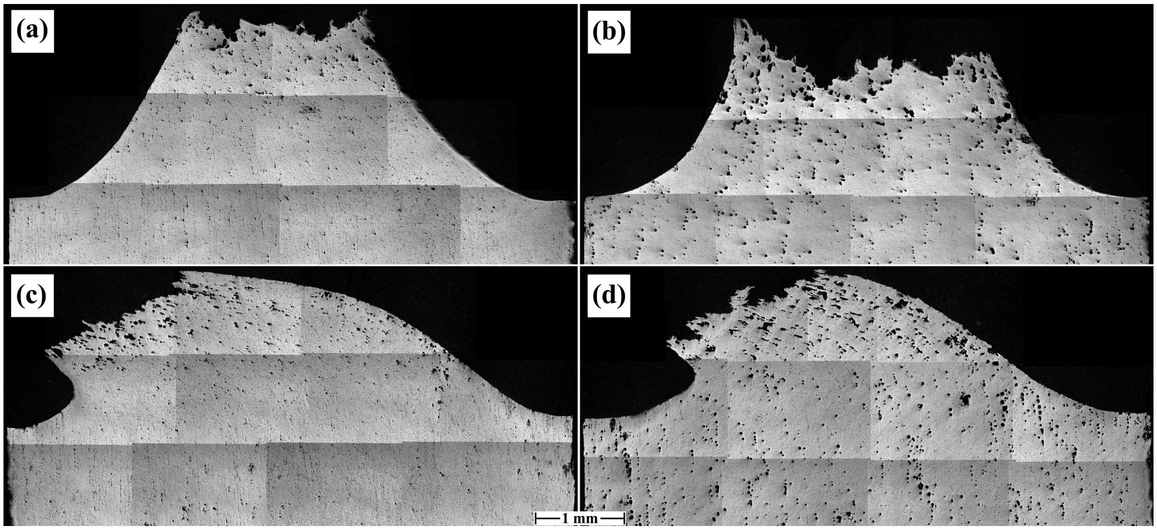


Fig. 12—Polished longitudinal cross sections of specimens tested to rupture under biaxial and triaxial conditions. (*a*) 7075 Al-L, triaxial tension, $\sigma_{nom}$ = 6.89 MPa; (*b*) 7075 Al-OH, triaxial tension, $\sigma_{nom}$ = 6.86 MPa; (*c*) 7075 Al-L, $\tau_{max}$ = 7.99 MPa; and (*d*) 7075 Al-OH, $\tau_{max}$ = 7.99 MPa. Each image is a montage of several optical micrographs, covering a large area near the rupture surface.

along particle stringers, were frequently observed in all samples (Figure 13(a)); (2) regardless of the type of heat treatment, a limited amount of cavities were found to have nucleated at cracks most likely formed in particles during primary processing (Figure 13(b)); (3) the majority of the cavities observed specifically in 7075 Al-OH had nucleated as a result of particle/matrix debonding (Figure 13(c)); and (4) most cavities observed in 7075 Al-L and 7075 Al-LT were found to have nucleated at particle/matrix interfaces (Figure 13(d)). It is important to note that cavities were also located at the shoulders of samples tested to failure.

The EDS analysis was conducted on a large number of the aforementioned cavity-nucleating particles. The presence of Fe was the common feature in spectrums obtained from all particles, and generally, regardless of the type of heat treatment, three types of spectrums were prominent (Figures 13(e) through (g)). The majority of the particles in all samples were represented by the spectrum shown in Figure 13(e). Based on available literature,[12,13] it appears that the particles represented by spectrums shown in Figures 13(e) and (f) are either $Al_7Cu_2Fe$ or $Al_{23}CuFe_4$, and those represented by the spectrum shown in Figure 13(g) are $(FeMnCr)_3SiAl_{12}$.

Figure 14, which shows SEM micrographs of the rupture surfaces of uniaxial specimens tested to failure under low (bottom row), intermediate (middle row), and high (top row) applied stresses, illustrates and compares the features observed in 7075 Al-L (left column), 7075 Al-LT (middle column), and 7075 Al-OH (right column). The figure shows that regardless of heat treatment or sample orientation (1) all alloys fail in a ductile manner, as characterized by the dimpled nature of the rupture surfaces; (2) the average dimple size increases with decreasing stress level; and (3) the depth and ridge sharpness of the dimples increases with increasing stress level. When compared at equivalent stress levels, it is evident that the average dimple size in 7075 Al-OH is significantly greater than that for 7075 Al-L and 7075 Al-LT. Also, it is important to add that closer examination of the interior of many dimples (at higher magnification) revealed the second-phase constituent particles responsible for cavity nucleation. An example of a 7075 Al-OH sample tested to failure at $\sigma$ = 10.5 MPa is shown in Figure 15. Particles located inside a dimple are clearly visible in this SEM micrograph.

## IV. DISCUSSION

### A. *High-Temperature Deformation*

The results obtained in the present investigation imply that, under existing testing conditions and regardless of heat treatment or sample orientation, 7075 Al seems to exhibit the characteristics of dislocation creep.[21] This is demonstrated by the following observations, which are common of all three sample types studied: (1) the presence of both an instantaneous strain upon loading and a relatively extensive decelerating primary stage, (2) a creep stress exponent of approximately 5.3, and (3) the dislocations tending to form simple sub-boundaries and dislocation arrays during creep. Despite these correlations, there are issues that require further examination before a conclusion can be drawn regarding the mechanism controlling creep deformation in the alloy.

Results obtained in numerous investigations[22,23,24] indicate that suitably processed 7000 series Al alloys possess a degree of superplasticity during creep deformation. Apart from an elevated testing temperature ($T > 0.5\ T_m$, where $T_m$ is the melting point), the main requirement for the occurrence of superplasticity (the ability of materials to exhibit extensive neck-free elongations) is a stable grain size, usually less than 10 $\mu$m. On this basis, samples tested in the annealed condition ($T$ = 648 K $> 0.5\ T_m$ and $d$ = 10 $\mu$m) would be expected to behave superplastically. An important characteristic of creep deformation in superplastic alloys is the experimental observation of a sigmoidal relationship between the applied stress and creep rate, which is distinguished by the presence of three regions of behavior:[25,26] region I (the low-stress region, with $n$ typically greater than 3), region II (the intermediate-stress or superplastic region where maximum ductility is observed; with $n < 2.5$), and region III (the high-stress region, with $n > 3$). The absence of such a sigmoidal trend is apparent in 7075 Al under

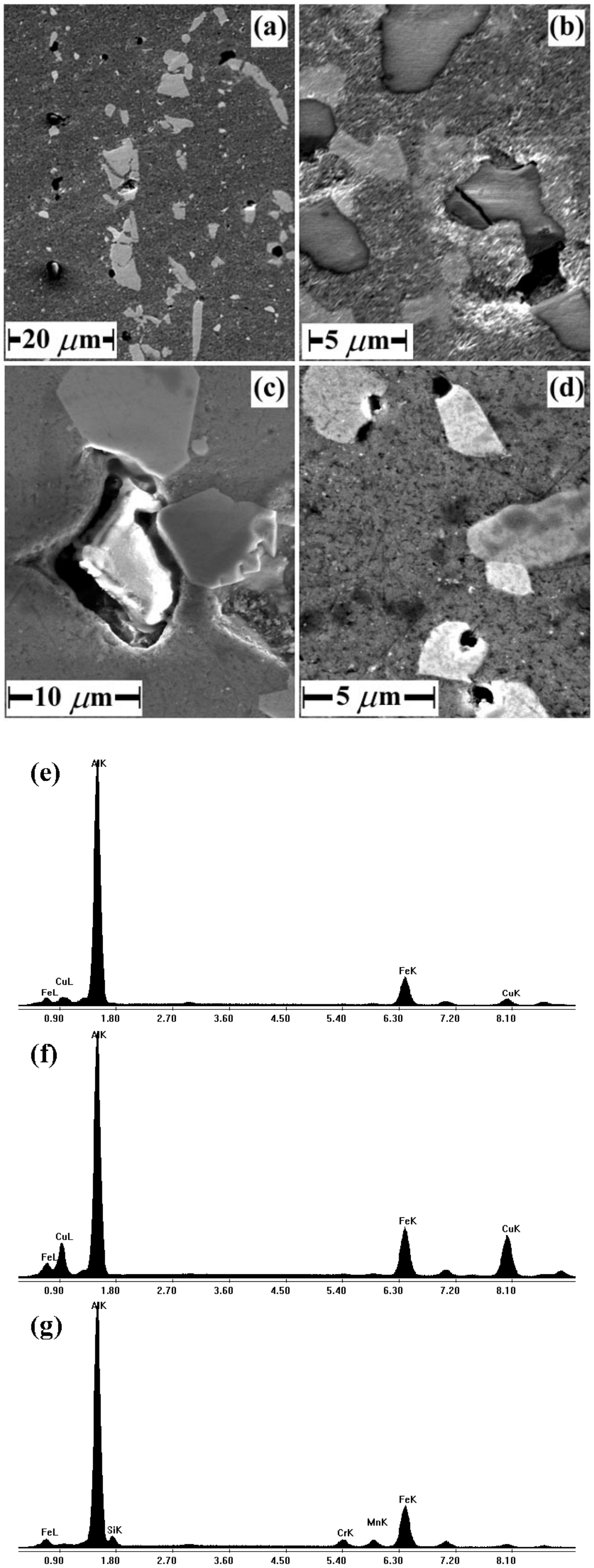


Fig. 13—Representative SEM micrographs showing cavity nucleation at second-phase constituent particles in (*a*) 7075 Al-L, (*b*) 7075 Al-L, (*c*) 7075 Al-OH, and (*d*) 7075 Al-LT. Samples were tested at intermediate stress levels, with regions of examination located at least 1.5 mm away from the rupture surface. (*e*) to (*g*) EDS spectrums for cavity nucleating particles in 7075 Al.

present experimental conditions ($n \sim 5.3$ over the entire stress range (Figure 7)). This is further demonstrated in Figure 16, where the creep data obtained elsewhere for 7075 Al($d = 12$ $\mu$m)[24] and 7475 Al ($d = 11$ $\mu$m)[22] are compared with those obtained for annealed 7075 Al in the present investigation. Examination of Figure 16 reveals a pattern, which can be utilized to explain the behavior observed in annealed 7075 Al. It is clearly evident that the slope of region II increases with decreasing testing temperature, and apparently, region III is extended to lower stress levels at the expense of region II. Ultimately, at the lowest testing temperature, only region III behavior is observed. Unlike deformation in region II, where creep characteristics appear to be consistent with the predictions of models that are based on GBS accommodated by some form of diffusion process,[27–31] deformation in region III is largely facilitated by dislocation creep mechanisms.[32] Therefore, the dislocation creep characteristics observed in the present study may be interpreted on this basis. However, it should be noted that the results of GBS measurements[32] conducted on various superplastic materials indicate that GBS still contributes almost 30 pct of the total strain in region III. Thus, GBS still has an active role in affecting creep deformation when $n > 3$.

The preceding discussion suggests that the deformation behavior of 7075 Al is consistent with the characteristics of region III of the sigmoidal relation between applied stress and creep rate. Further support for this suggestion is provided by the following correlation. It has been demonstrated that for both superplastic Pb-62 wt pct Sn and Zn-22 wt pct Al alloys, the transition from the superplastic region II to the high stress region III occurs when the grain size of the material, $d$, is equal to the subgrain size $\delta$.[33] As reported elsewhere,[21,34] the subgrain size is dependent on the applied stress through an experimental relationship of the following form:

$$\frac{\sigma}{G} = 20\left(\frac{\delta}{\mathbf{b}}\right)^{-1} \qquad [10]$$

where $G$ is the shear modulus and $\mathbf{b}$ is the burgers vector. Using $\delta = d = 10$ $\mu$m, $\mathbf{b} = 2.86 \times 10^{-8}$ cm, and the value of $G$ for Al at 648 K leads to $\sigma = 11$ MPa, a value which is very close to the lowest value of applied stress used in the present investigation on 7075 Al.

Based on the present microstructural observations (Figure 2), it is likely that the dense population of coarse and plateletlike precipitates, which uniformly decorate the grain boundaries in 7075 Al-OH, would inhibit boundary sliding at the relatively low testing temperatures utilized in the present investigation. The influence of GBS on creep deformation may be characterized by the stress enhancement factor, $f$. In the presence of GBS, the creep rate of the bulk material can be expressed as

$$\dot{\varepsilon}_{\min} = A(f\sigma)^n \qquad [11]$$

The stress enhancement factor is a volume-averaged measure of stress elevation arising from GBS due to load transfer from the sliding-inclined boundaries to regions of the microstructure where sliding does not occur. In the absence of GBS (7075 Al-OH), the bulk material deforms uniformly ($f = 1$) and the minimum creep rate is given by Eq. [7]. The results in Figure 7 indicate that $f = 1.48$ for annealed

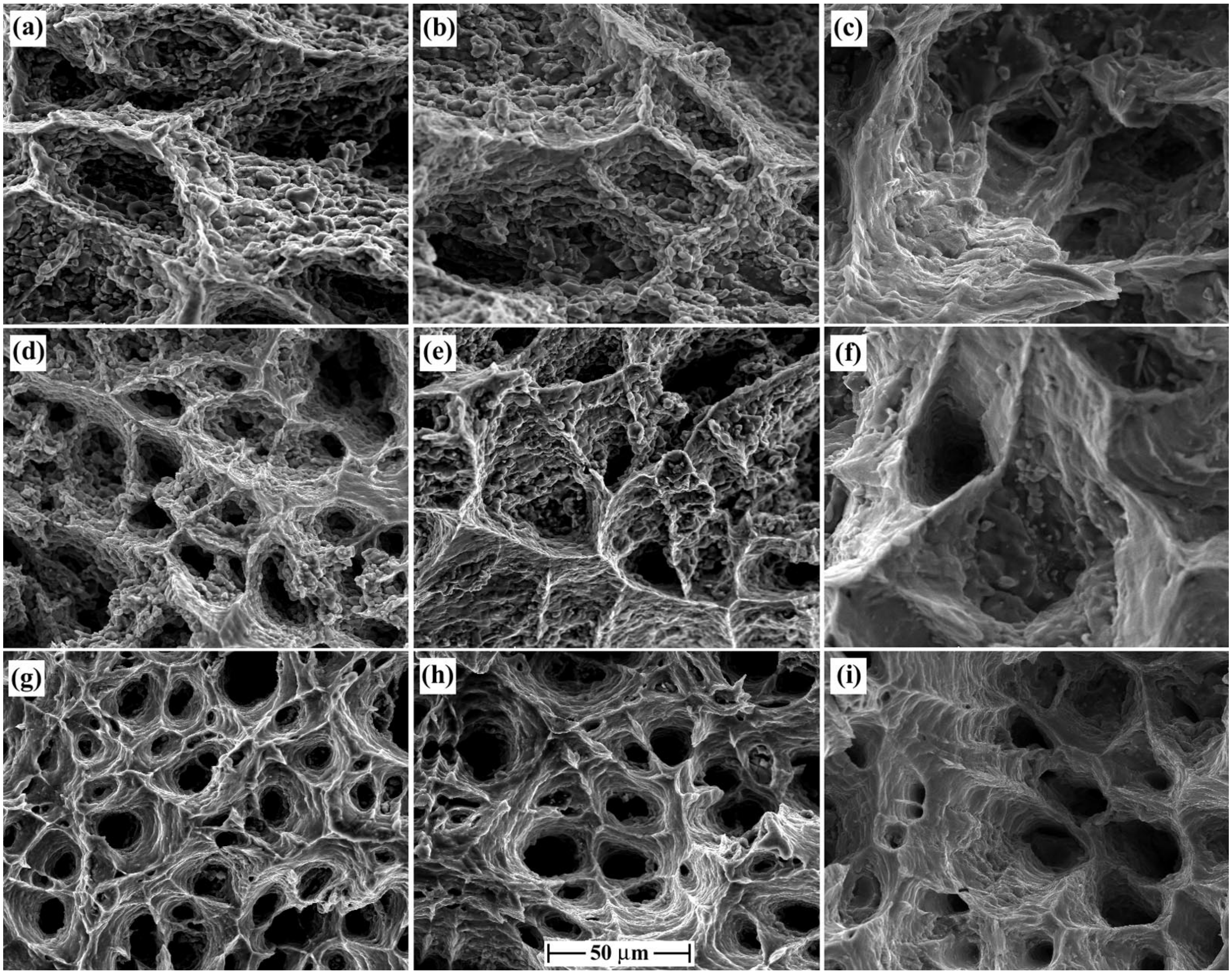


Fig. 14—SEM micrographs of the rupture surfaces of uniaxial specimens tested to failure under low, intermediate, and high applied stresses. (*a*) 7075 Al-L, $\sigma = 8.86$ MPa; (*b*) 7075 Al-LT, $\sigma = 8.87$ MPa; (*c*) 7075 Al-OH, $\sigma = 8.89$ MPa; (*d*) 7075 Al-L, $\sigma = 12.21$ MPa; (*e*) 7075 Al-LT, $\sigma = 13.64$ MPa; (*f*) 7075 Al-OH, $\sigma = 12.24$ MPa; (*g*) 7075 Al-L, $\sigma = 29.7$ MPa; (*h*) 7075 Al-LT, $\sigma = 29.7$ MPa; and (*i*) 7075 Al-OH, $\sigma = 25.5$ MPa.

7075 Al assuming that GBS is prevented in the overheated microstructure as a result of the observed particles on the boundaries.

Several researchers have studied the effects of GBS on overall creep rates using finite element methods.[35,36,37] For example, Gharemani[35] developed a two-dimensional (2-D) model of hexagonal grains deforming by steady-state creep and GBS. This model predicts a value of $f$ equal to 1.2 for $n = 5$. Dib and Rodin[36] developed a three-dimensional (3-D) steady-state creep model that incorporates Wigner–Seitz cells as grains. Their results also predict a stress enhancement factor of 1.2 for a statistical array of grains and $3 \leq n \leq 8$. Similarly, Chakraborty and Earthman[37] also calculated $f = 1.2$ for $n = 5$ with a hexagonal grain model of both primary and secondary creep deformation in conjunction with GBS. Thus, $f \cong 1.2$ is uniformly predicted by several models of dislocation creep coupled with GBS for both 2-D and 3-D grain configurations.

The present experimental results shown in Figure 7 imply a value of $f$ equal to approximately 1.5 if GBS is suppressed in the overheated microstructure. Therefore, it appears that the difference in minimum creep rate between the annealed and overheated microstructures cannot be completely accounted for by the effect of GBS, as predicted by finite

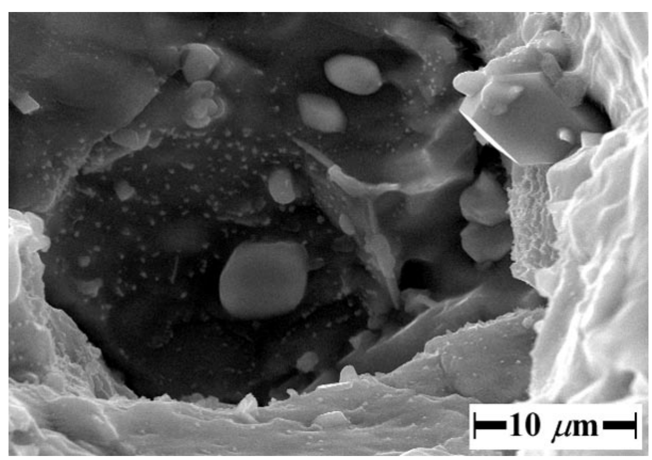


Fig. 15—SEM micrograph at higher magnification revealing the interior of a dimple and the second-phase constituent particles responsible for cavity nucleation (7075 Al-OH, uniaxial tension, $\sigma = 10.5$ MPa).

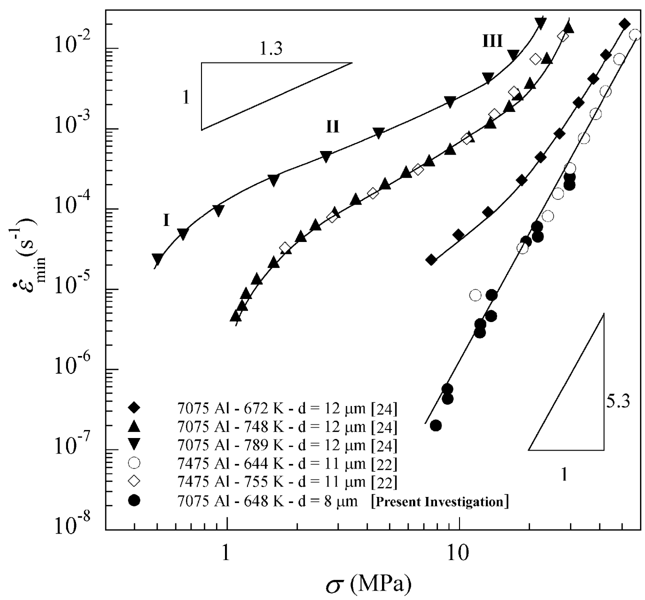


Fig. 16—A comparison between creep data obtained elsewhere for 7075 Al ($d$ = 12 $\mu$m)[24] and 7475 Al ($d$ = 11 $\mu$m)[22] and those obtained for annealed 7075 Al in the present investigation.

element techniques. However, it should be noted that none of the aforementioned models allow for any cavities at the triple junctions constraining GBS. Chakraborty and Earthman[38] have developed finite element creep models that incorporate cavitation as well as GBS. Their results in comparison to their earlier results indicate that the stress enhancement due to GBS increases somewhat when cavities are allowed to form. In effect, the cavities extend the regions undergoing GBS, which then redistribute more stress to the regions that deform only by dislocation creep. Thus, it follows that $f$ values predicted by the models that do not include cavitation represent a lower bound estimate, and an observation of $f \cong 1.5$ is reasonable given that some cavities at triple junctions will have already nucleated prior to reaching the minimum creep rate. This finding combined with microstructural observations of large particles on grain boundaries in the overheated microstructure provides further evidence for the notion that the difference in creep rate between the overheated and annealed samples is primarily due to the effect of GBS. A simple stress enhancement, as opposed to a total change in rate-limiting deformation mechanism, is also consistent with the observation that both microstructures exhibit the same stress exponent, $n \cong 5$, also evident in Figure 7.

The previous discussion emphasizes that while GBS contributes to creep deformation in annealed 7075 Al, it does not play a significant role in 7075 Al-OH. Bearing this in mind, attention is now focused on high-temperature rupture behavior in 7075 Al.

### B. *High-Temperature Rupture*

The detailed microstructural observations made in the present investigation indicate that cavitation damage is the dominant failure mechanism in 7075 Al. Optical microscopy (Figures 11 and 12) revealed that, regardless of heat treatment, sample orientation, stress level, or stress state, extensive cavitation occurred in all samples and was not limited to the vicinity of the fracture surfaces. Scanning electron microscopy, which was utilized primarily to identify cavity nucleation sites (Figures 13 and 15), also revealed cavities located at the shoulders of samples tested to failure (experiencing ~25 pct of the applied stress), providing further evidence for the dominance of cavitation damage. The dimpled nature of the fracture surfaces (Figure 14) also indicates that failure resulted from extensive cavitation.

Early studies[18] suggested that creep life under multiaxial stress states can be predicted using either $\sigma_1$, when cavities nucleate readily and distribute homogeneously on all grain boundaries, or $\sigma_e$, when failure is primarily due to changes in the internal dislocation structure. Accordingly, the creep-damage tolerance parameter (Section III–C) was thought to provide a simple means of predicting multiaxial creep rupture characteristics.[39] For example, when $1 < \lambda < 2.5$, it was proposed that creep rupture should be controlled by diffusive cavitation making $\sigma_1$ the appropriate representative stress parameter. Furthermore, substructural softening is thought to become dominant when $\lambda$ takes on larger values ($\lambda > 5$), and $\sigma_e$ should be considered as the correlating stress parameter for rupture time. On this basis, the results shown in Figure 9 would lead to the following expectations. First, creep rupture in annealed 7075 Al is due to diffusion-controlled cavitation, since data for 7075 Al-L and 7075 Al-LT clearly fall within the $1 < \gamma < 2.5$ region, and $\sigma_1$ should be used to predict multiaxial rupture. Second, the $\gamma$ values for 7075 Al-OH lie above the cavitation-controlled region but are less than 5, which represents the typical limit above which strain softening dominates. Therefore, it is reasonable that creep rupture time of 7075 Al-OH depends on both $\sigma_1$ and $\sigma_e$ (Section III–C). However, the results obtained in the present investigation indicate that this simple picture has limited accuracy. While microstructural observations of widespread cavitation lend support to the first expectation, it is clearly evident that the maximum principal stress parameter fails to correlate the data for 7075 Al-L and 7075 Al-LT (Figure 10). In addition, even though the rupture data for 7075 Al-OH provide indirect support for the second expectation by showing that neither $\sigma_1$ nor $\sigma_e$ correlate the data satisfactorily when acting alone, less extensive cavitation would be anticipated, due to the increased contribution of $\sigma_e$. This clearly contrasts with the cavitational features observed in 7075 Al-OH (Figures 11, 12, and 14). Similar inconsistencies have also been noted in other investigations,[40,41] where observed values for $\lambda$ have not been able to match experimental/theoretical expectations. Accordingly, two other stress parameters derived for situations where a large number of cavities interact with particular deformation processes were also considered.

It was found that the principal facet stress parameter correlates the rupture times for annealed 7075 Al to a correlation coefficient of 0.95, bringing the data for three stress states onto a single curve (Figure 10). On the other hand, it was observed that $\sigma_C$ provides the best correlation for the same alloy but in an overheated condition (Figure 10). As discussed earlier, microstructural evidence of widespread cavitation in the alloy (Figure 11 through 14) also lends strong support for the validity of these parameters. The success of $\sigma_F$ implies that cavitation in 7075 Al-L and 7075 Al-LT is coupled with either GBS or other localized deformation processes along inclined directions such as rapid creep within PFZs. By contrast, the success of $\sigma_C$ suggests that cavitation in 7075 Al-OH is constrained by relatively uniform creep deformation, and the driving force for cavity growth is therefore determined primarily by the rate of dislocation creep within the matrix of the grains.

The principal facet stress was found to provide the best correlation of multiaxial rupture data for a wide range of engineering alloys in earlier studies.[20,40,42] The rationale for the success of this parameter has been the operation of at least one localized deformation mechanism, such as GBS or rapid creep within PFZs that facilitate stress redistribution to cavitating boundaries.[20] It is interesting to point out that both highly localized deformation modes may be operative for the present annealed alloy. While the results in Section IV–A provide clear evidence of the contribution of GBS to creep deformation in the alloy, microstructural observations (Figure 2) imply that localized deformation within the softened PFZs may also play a role. These findings substantiate the success of the principal facet stress in correlating the rupture data for 7075 Al-L and 7075 Al-LT. By contrast, $\sigma_C$, rather than $\sigma_F$, provides better correlation for 7075 Al-OH. This failure of $\sigma_F$ may be related to the absence of GBS in the 7075 Al-OH, which contains relatively large particles on the grain boundaries.

Under conditions of unconstrained grain boundary cavitation, it is assumed that cavity growth can readily be accommodated by concurrent creep deformation. The cavity growth rate, which consists of both diffusion and plasticity-controlled components, becomes constrained if it is faster than the creep rate of the surroundings.[43] In coarse-grained 7075 Al-OH, the large variations in strength between the wide PFZs and the surrounding material may significantly enhance the plasticity-controlled component, leading to constrained cavity growth rates. Consequently, in a manner that is envisaged in the derivation of $\sigma_C$, grain boundary cavitation in 7075 Al-OH becomes constrained by creep deformation of the surroundings.

Microstructural observations (Section III–C) indicate that the large majority of the cavities observed in 7075 Al-OH form at large second-phase constituent particles (due to particle/matrix debonding). As expected, the heterogeneous distribution of cavities in 7075 Al-OH (Figures 11(e) and (f)) was also found to correspond directly with that of coarse (5 to 25 $\mu$m) second-phase constituents (Figure 1(f)). Regions of extensive cavitation were located along the particle stringers, with insignificant cavitation occurring in the particle-free regions in between. It would be reasonable to assume that the cavity growth rate within the particle-rich regions is faster than the creep rate of the adjacent particle-free regions. On this basis, it appears that, as a result of stress redistribution, cavity growth rates in 7075 Al-OH may be constrained by creep deformation within the relatively large particle-free (cavity-free) regions.

The preceding discussion highlights the general applicability of the approach utilized in the present investigation. The principal advantage of this approach lies in the fact that the geometry of the samples used to generate multiaxial rupture data (Table II) is simple, and tests are performed using conventional creep testing apparatus. Results can successfully be applied to identify both the suitable representative stress parameter for predicting creep life of components under complex loading conditions and the governing creep rupture mechanism in the alloy under investigation.

## V. CONCLUSIONS

High-temperature deformation and rupture behavior of commercial 7075 Al was investigated at 648 K, under uniaxial, biaxial, and triaxial stress states. Annealed and overheated samples were tested in longitudinal and long transverse directions, providing means of investigating the influence of both microstructure and orientation on multiaxial creep rupture behavior in the alloy.

Experimental data, which cover over four orders of magnitude of strain rate, indicate that 7075 Al, under present testing conditions and regardless of heat treatment or sample orientation, seems to exhibit deformation characteristics that are consistent with region III of the sigmoidal relationship observed during superplastic deformation. This was manifested by (1) the presence of both an instantaneous strain upon loading and a relatively extensive decelerating primary stage, (2) a creep stress exponent of almost 5.3, and (3) the dislocations tending to form simple sub-boundaries and dislocation arrays during creep. While the results imply the presence of a concomitant contribution from GBS during creep deformation in the annealed condition, creep rates for overheated 7075 Al suggest that GBS is suppressed. This hypothesis is supported by the observations of large particles at grain boundaries in the overheated microstructure and boundaries containing few or no particles on boundaries in the annealed microstructure.

Rupture times for different stress states have been compared with respect to different physically based multiaxial stress parameters, each of which is linked to a particular physical mechanism known to control the creep rupture process. It was shown that neither the maximum principal stress nor the von Mises effective stress could satisfactorily correlate the rupture data for 7075 Al. While the rupture time for annealed 7075 Al (regardless of sample orientation) was successfully correlated by the principal facet stress parameter, it was found that $\sigma_C$, based on the constrained cavity growth model of Rice, offers the best correlation for the alloy tested in the overheated condition.

The success of these parameters has two major implications. First, creep rupture in annealed 7075 Al (regardless of sample orientation) is dominated by cavitation coupled with GBS. Second, creep rupture of the overheated microstructure is dominated by cavitation that is constrained by relatively uniform creep deformation in the matrix. Therefore, the primary mechanism for both creep deformation and cavity growth in the overheated 7075 Al is determined by dislocation creep in the matrix that is not coupled with GBS. By contrast, both dislocation creep and GBS appear to have important roles in governing the creep rate and rupture time of the annealed samples.

## ACKNOWLEDGMENTS

This work was supported, in part, by the United States Department of Energy under Grant No. DE-FG03-90ER45420 and, in part, by the National Science Foundation under Grant No. DMR-9810422.

## REFERENCES


1. H. Riedel: in *Fracture at High Temperatures*, B. Ilschner and N. Grant, eds., MRE Springer-Verlag, New York, NY, 1986.
2. M.F. Ashby and B.F. Dyson: *Proc. 6th Int. Conf. on Fracture ICG6*, S.R. Valluri, D.M.R. Taplin, P. Rama Rao, J.F. Knott, and R. Dubey, eds., Pergamon, New Delhi, India, 1984, vol. 1, pp. 3-30.
3. A.S. Argon: in *Recent Advances in Creep and Fracture of Engineering Materials and Structures*, B. Wilshire and D.R. Owen, eds., Pineridge Press, Swansea, United Kingdom, 1982, pp. 1-52.
4. D.R. Hayhurst: *J. Mech. Phys. Solids*, 1972, vol. 20, pp. 381-90.
5. D.R. Hayhurst and F.A. Leckie: *Proc. 4th Int. Conf. on the Mechanical Behaviour of Materials*, J. Carlsson and N.G. Ohlson, eds., Pergamon Press, Stockholm, 1984, vol. 2, pp. 1195-1211.
6. R.J. Browne, D. Lonsdale, and P.E.J. Flewitt: *Trans. ASME, J. Eng. Mater. Technol.*, 1982, vol. 104, pp. 291-96.
7. B.J. Cane: *Acta Metall.*, 1981, vol. 29, pp. 1581-91.
8. R.L. Huddleston: *Trans. ASME, J. Pressure Vessel Technol.*, 1985, vol. 107, pp. 421-29.
9. D.R. Hayhurst, F.A. Leckie, and J.T. Henderson: *Int. J. Mech. Sci.*, 1977, vol. 19, pp. 147-59.
10. H.-K. Kim, F.A. Mohamed, and J.C. Earthman: *J. Testing Eval.*, 1991, vol. 19, pp. 93-96.
11. N.L. Johnson and J.C. Earthman: *J. Testing Eval.*, 1994, vol. 22, pp. 111-16.
12. R. Ayer, J.Y. Koo, J.W. Steeds, and B.K. Park: *Metall. Trans. A*, 1985, vol. 16A, pp. 1925-36.
13. M. Gao, C.R. Feng, and R.P. Wei: *Metall. Mater, Trans. A*, 1998, vol. 29A, pp. 1145-51.
14. J.A. Wert, N.E. Paton, C.H. Hamilton, and M.W. Mahoney: *Metall. Trans. A*, 1981, vol. 12A, pp. 1267-76.
15. X. Yang, H. Miura, and T. Sakai: *Mater. Trans. JIM*, 1996, vol. 37, pp. 1379-87.
16. J. Liu and D.J. Chakrabarti: *Acta Mater.*, 1996, vol. 44, pp. 4647-61.
17. B.F. Dyson and T.B. Gibbons: *Acta Metall.*, 1987, vol. 35, pp. 2355-69.
18. A.E. Johnson, J. Henderson, and B. Khan: *Complex Stress Creep, Relaxation and Fracture of Metallic Alloys*, HMSO, Edinburgh, 1962.
19. J.R. Rice: *Acta Metall.*, 1981, vol. 29, p. 81.
20. W.D. Nix, J.C. Earthman, G. Eggeler, and B. Ilschner: *Acta Metall.*, 1989, vol. 37, pp. 1067-77.
21. J.E. Bird, A.K. Mukherjee, and J.E. Dorn: in *Quantitative Relation between Microstructure and Properties*, D.G. Brandon and A. Rosen, eds., Israel Universities Press, Haifa, 1969, pp. 255-342.
22. N.E. Paton, C.H. Hamilton, J. Wert, and M. Mahoney: *J. Met.*, 1982, vol. 34, pp. 21-27.
23. C.H. Hamilton, C.C. Bampton, and N.E. Paton: in *Superplastic Forming of Structural Alloys*, N.E. Paton and C.H. Hamilton, eds., TMS-AIME, San Diego, CA, 1982, pp. 173-89.
24. P. Malek: *Mater. Sci. Eng. A*, 1991, vol. A137, pp. 21-26.
25. F.A. Mohamed and T.G. Langdon: *Acta Metall.*, 1975, vol. 23, pp. 117-24.
26. F.A. Mohamed and T.G. Langdon: *Phil. Mag.*, 1975, vol. 32, pp. 697-709.
27. A. Ball and M.M. Hutchinson: *Met. Sci. J.*, 1969, vol. 3, pp. 1-7.
28. A.K. Mukherjee: *Mater. Sci. Eng.*, 1971, vol. 8, pp. 83-89.
29. R.C. Gifkins: *Metall. Trans. A*, 1976, vol. 7A, pp. 1225-32.
30. J.H. Gittus: *Trans. ASME, H, J. Eng. Mater. Technol.*, 1977, vol. 99, pp. 244-51.
31. A. Arieli and A.K. Mukherjee: *Mater. Sci. Eng.*, 1980, vol. 45, pp. 61-70.
32. T.G. Langdon: *Metall. Mater. Trans. A*, 1982, vol. 13A, pp. 689-701.
33. F.A. Mohamed and T.G. Langdon: *Scripta Metall.*, 1976, vol. 10, pp. 759-62.
34. T.J. Ginter and F.A. Mohamed: *J. Mater. Sci.*, 1982, vol. 17, pp. 2007-12.
35. F. Ghahremani: *Int. J. Solids Struct.*, 1980, vol. 16, pp. 847-62.
36. M.W. Dib and G.J. Rodin: *J. Mech. Phys. Solids*, 1993, vol. 41, pp. 725-47.
37. A. Chakraborty and J.C. Earthman: *Metall. Mater. Trans. A*, 1997, vol. 28A, pp. 979-89.
38. A. Chakraborty and J.C. Earthman: *Acta Mater.*, 1997, vol. 45, pp. 4615-26.
39. F.A. Leckie: *Phil. Trans. R. Soc. London A*, 1995, vol. 351, pp. 611-23.
40. H.-K. Kim, F.A. Mohamed, and J.C. Earthman: *Metall. Trans. A*, 1991, vol. 22A, pp. 2629-36.
41. F.A. Leckie: *Eng. Fract. Mech.*, 1986, vol. 25, pp. 505-21.
42. H. Yu-Hsian, Z. Hongyan, and G.S. Daehn: *Metall. Mater. Trans. A*, 1996, vol. 27A, pp. 891-900.
43. B.F. Dyson: *Met. Sci.*, 1976, vol. 10, pp. 349-53.